Theoretical characterization of silicon self-interstitial clusters in uniform strain fields

Robert J. Bondi, Sangheon Lee, and Gyeong S. Hwang*

Department of Chemical Engineering, University of Texas, Austin, Texas 78712, USA

(Received 30 March 2009; revised manuscript received 28 June 2009; published 15 September 2009)

We use first-principles density-functional theory calculations to evaluate the orientation-dependent stability of small, neutral self-interstitial clusters (I_n, $n \leq 4$) in crystalline Si across a range of uniform strain conditions ($-4 \leq \varepsilon \leq 4\%$) in both uniaxial and biaxial strain fields on Si(100). Comprehending the behavior of these small clusters under strain is important in extending our understanding of the evolutionary cycle of interstitial defects during the ion implantation and annealing processes that occur during semiconductor manufacturing. Our calculation results suggest that strain of sufficient magnitude can contribute to significant ground-state structural distortion and even generation of different cluster configurations. Our study also indicates that the relative stability change per unit change in applied strain is greater in the biaxial case than the uniaxial case for interstitial clusters. We provide localized strain-distribution profiles and modification of bulk Si density of states to characterize the extent to which interstitial clusters modulate crystalline Si structure.

DOI: 10.1103/PhysRevB.80.125202 PACS number(s): 61.72.−y

I. INTRODUCTION

Strain engineering is a useful technique to modify many important material properties and effectively create new advanced materials. For electronic applications, strain engineering has received intense attention in the semiconductor industry over the last decade as a low-cost, easily-integrated method to extend silicon complementary metal-oxide semiconductor (CMOS) transistor performance.[1] Consequently, the semiconductor industry began widely incorporating process-induced strain into manufacturing flows with the introduction of the 90 nm node as a cost effective technique to help extend transistor performance improvement consistent with Moore's Law.

Ion implantation creates Si self-interstitial defects that are associated with transient-enhanced diffusion of dopants during postimplantation annealing, which results in degradation of dopant profiles that are critical in the formation of ultrashallow junctions. Small interstitial clusters are also thought to be involved in the evolution of {311}-extended defects.[2–5] Recent experimental work has succeeded in providing further insight into the behavior of small interstitial clusters using techniques such as deep-level transient spectroscopy and photoluminescence spectroscopy from ion-implanted Si substrates.[2,3] Numerous, recent publications acknowledge the general trend that interstitial clusters become more stable as size increases, as well as the particularly stable local minima structures observed at $n=4$ and $n=8$.[2,6,7] We hope to expand this field further by characterizing the orientation-dependent stability of small, neutral interstitial cluster configurations (I_n, $n \leq 4$) and orientations under various types of uniform strain conditions. These small clusters are of importance as either highly mobile species during high-temperature annealing processes (I_n, $n=1$ and 2) and/or as constituent components of larger clusters.

There are two ways of technological relevance to apply strain to the channel of a metal-oxide semiconductor field-effect transistor (MOSFET): biaxial strain, which is sometimes called global or bulk strain because it is implemented at the substrate level, and uniaxial strain, which is sometimes referenced as local or process-induced strain.[8] Tensile biaxial strain can be implemented in a transistor channel by building the entire device in strained Si epitaxy over a thick $Si_{1-x}Ge_x$ layer. Uniaxial strain is often implemented at the device level in two ways: (1) selective epitaxial growth of a binary Si alloy ($Si_{1-x}Ge_x$ for channel compression and $Si_{1-x}C_x$ for channel tension) in the source/drain recessed regions to impose strain along the transistor channel direction or (2) deposition of a high-stress silicon nitride cap layer which mechanically couples the local strain of the film into the underlying transistor channel. Hydrostatic strain can be achieved in bulk Si simply by subjecting the material to a uniform pressure field, but this form is technologically less relevant than biaxial or uniaxial strain.

For technological applications, uniaxial strain is likely most prevalent as it is preferred in most CMOS processes for ease of manufacturability and better electrical performance return.[1,9] Major applications for biaxial strain include devices with heterojunctions such as heterojunction bipolar transistors and modulation-doped field effect transistors (MODFETs) for analog microwave circuits.[10] Biaxial strain also appears promising for fabricating fully-depleted CMOS devices using strained silicon-on-insulator substrates.[11] Hydrostatic strain is rarely, if ever, used in device applications, but it is conceivable that localized, nonuniform hydrostatic strain fields could exist inside developing new material systems such as embedded Si nanocrystals.[12,13] For the purpose of comparison, we selectively include results for interstitial clusters subjected to hydrostatic strain conditions.

In this paper, we examine the model case of small interstitial Si clusters in a uniform strain field, which might occur in the middle of a MOSFET transistor with a ⟨110⟩-aligned channel. A (100) wafer orientation is also used in our atomistic models because this substrate is dominant in CMOS manufacturing. The generation of most clusters (I_n, $n \geq 3$) studied was accomplished using the integrated atomistic modeling procedure of Lee and Hwang[14–16] which combines continuous random network model-based Metropolis Monte Carlo, tight-binding molecular-dynamics, and density-functional theory (DFT) simulations.

 ©2009 The American Physical Society

II. COMPUTATIONAL METHODS

All optimized atomic structures and energies reported herein were computed using a plane-wave basis set pseudopotential method within the generalized gradient approximation of Perdew and Wang (GGA-PW91) (Refs. 17 and 18) to DFT,[19] as implemented in the well-established Vienna *ab initio* simulation package (VASP).[20] Vanderbilt-type ultrasoft pseudopotentials[21] were used for core-electron interactions. Outer electron wave functions were expanded using a plane-wave basis set with a kinetic-energy cutoff of 160 eV. The Brillouin-zone sampling was performed with one k-point (Γ) for geometric optimization. The geometric optimization allowed all atoms to relax until the total energy had converged within 1×10^{-3} eV tolerance. With the optimized ionic positions determined, corresponding total energies were refined using a $(2\times2\times2)$ Monkhorst-Pack grid. For density of states (DOS) near the Si band gap, subsequent VASP simulations were conducted on the optimized ionic configurations with the Monkhorst-Pack mesh increased $(4\times4\times4)$ and charge smearing modeled with the tetrahedron method.[20] For the strain-free supercell, we used a fixed Si lattice constant of 5.457 Å along $\langle 100\rangle$ or 3.859 Å along $\langle 110\rangle$ as obtained from volume optimization. To evaluate uniaxial, biaxial, and hydrostatic strain conditions, we computed a basis set of lattice vectors associated with a four-atom supercell for each strain condition $(-4\leq\varepsilon\leq4\%)$ and scaled the basis set up to each supercell size investigated. Most clusters reported in this work were embedded inside 256-atom supercells, while the larger clusters $(n>4)$ required 480-atom supercells. We found that different cluster orientations often shift the qualification of adequate supercell size to avoid periodic image effects. In addition, fourfold-coordinated clusters typically generate local tensile strain fields that decay slowly away from the cluster. To avoid excessively large supercell sizes, we equated the formation energies for all orientations at the strain-free condition to reference the lowest strain-free formation energy found. This same formation-energy reference shift was then applied to all strain conditions for a given configuration. All supercells used have two independent $\{110\}$ facets and one independent $\{100\}$ facet to model (100)-oriented Si with CMOS transistor channels aligned along a $\langle 110\rangle$ direction [Fig. 1]. Perl scripts were generated to facilitate and manage executing repeated VASP simulations across the range of strain conditions studied for each of the three types of uniform strain considered.

To calculate modified lattice constants for biaxially strained Si, we can quantify the Poisson effect, as visually depicted in Fig. 1(a), by defining a quantity, ν^*, that relates the ratio of in-plane strain, $\varepsilon_\parallel$, and out-of-plane strain, $\varepsilon_\perp$. Additional theoretical background for biaxial strain was previously published.[22] In our system, the values of $a_\parallel$ in Si under tensile strain conditions are equal to representative values of a_{SiGe}, which is the lattice constant of a binary SiGe system. We calculate the in-plane strain as $\varepsilon_\parallel=(a_{SiGe}-a_{Si})/a_{Si}$ and the out-of-plane strain as $\varepsilon_\perp=(a_\perp-a_{Si})/a_{Si}$. The experimental value of a_{Si} is 5.4309 Å and a_{Ge} is 5.6461 Å,[23] so 4% tensile strain is the limiting case of Si grown over pure Ge. From linear elastic theory,[23–26] the relationship between out-of-plane and in-plane strain for a cubic crystal can be expressed in terms of two elastic stiffness constants,

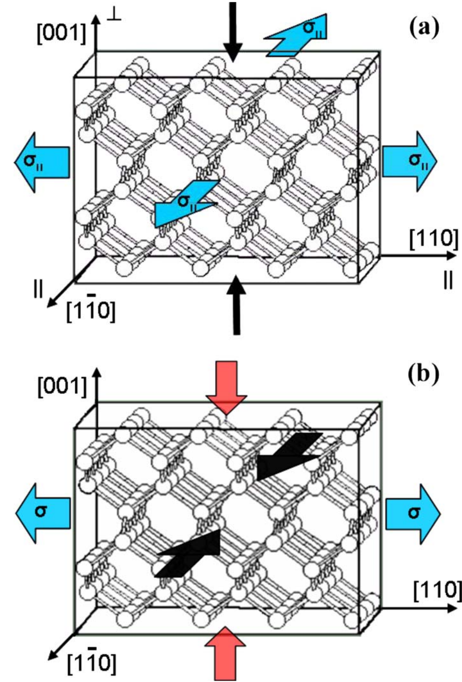

FIG. 1. (Color online) (a) Tensile biaxial stress/strain interaction in our model Si supercell. In the figure, applied tensile stress, $\sigma_\parallel$, in the plane of the substrate acts equally in all directions as shown by block arrows and produces a tensile strain. In response, the lattice contracts in the out-of-plane direction as shown by the solid black arrows. Under compressive strain conditions, the directions of all arrows are inverted. (b) Tensile uniaxial stress/strain interaction in our model Si supercell. For this case, tensile stress, σ, is independently applied along [110] and results in a corresponding strain along [110]. In response, the lattice dependently contracts along both $[1\bar{1}0]$ (black arrows) and [001] (red arrows) but the magnitude of the contractions will be different as determined by the respective Poisson ratios. Under compressive conditions, the directions of all arrows are inverted.

$$\nu^* = -\varepsilon_\perp/\varepsilon_\parallel = 2(C_{12}/C_{11}). \quad (1)$$

Using tabulated values[27] for C_{11} and C_{12}, the value of ν^* is 0.771. Using ν^* and the expressions for $\varepsilon_\parallel$ and $\varepsilon_\perp$, we calculated the values of $a_\perp$ for each independent value of $a_\parallel$ studied. All results presented for biaxially strained Si are based on $\nu^*=0.771$.

Calculating modified lattice constants for uniaxially strained Si is more involved than the biaxial case because it is necessary to determine the Poisson ratios (ν) for two pairs of independent crystal directions. A visualization of a Si supercell experiencing uniaxial strain is provided in Fig. 1(b). In this case, an independent stress, $\sigma_{[110]}$, results in a corresponding strain, $\varepsilon_{[110]}$. In response, the crystal lattice will experience strain deformation of opposite sign along both $[1\bar{1}0]$ and [001], but the magnitude of strain in these directions will be different because of the anisotropic nature of the crystal. To estimate the magnitudes of both dependent

strains, $\varepsilon_{[1\bar{1}0]}$ and $\varepsilon_{[001]}$, the ν between [110] and $[1\bar{1}0]$ and the ν between [110] and [001] must be calculated. Brantley[28] derived a generalized expression using tensor mathematics to compute ν between two arbitrary crystallographic directions in a cubic crystal using elastic compliances,

$$\nu = -\frac{s_{12} + \left(s_{11} - s_{12} - \frac{1}{2}s_{44}\right)[l_1^2 m_1^2 + l_2^2 m_2^2 + l_3^2 m_3^2]}{s_{11} - 2\left(s_{11} - s_{12} - \frac{1}{2}s_{44}\right)[l_1^2 m_2^2 + l_2^2 m_3^2 + l_1^2 m_3^2]}, \quad (2)$$

where $s_{\rm ij}$ are the three independent elastic compliances for a cubic system and $\mathbf{l}_{\rm i}$ and $\mathbf{m}_{\rm i}$ are direction cosines for $\mathbf{l}$ (independent strain direction) and $\mathbf{m}$ (dependent strain direction), respectively, relative to the $\langle 100 \rangle$ directions.

Using Brantley's expression, we computed the desired Poisson ratios as follows:

$$\nu_{[110],[001]} = -\frac{\varepsilon_{[001]}}{\varepsilon_{[110]}} = 0.361, \quad (3)$$

$$\nu_{[110],[1\bar{1}0]} = -\frac{\varepsilon_{[1\bar{1}0]}}{\varepsilon_{[110]}} = 0.064. \quad (4)$$

These arithmetically computed values are consistent with graphical results published by Wortman and Evans.[29] With the Poisson ratios known and $\varepsilon_{[110]}$ independently defined as the percent strain imposed on the system, $\varepsilon_{[1\bar{1}0]}$ and $\varepsilon_{[001]}$ are easily determined. With the strain relationships between crystallographic directions identified, it is relatively straightforward to tabulate uniaxially-modified values of $a_{[1\bar{1}0]}$ and $a_{[001]}$ for each independent value of $a_{[110]}$ studied.

Modeling hydrostatic strain conditions is identical to simulating a uniform pressure field applied to the material system. Since this case is inherently isotropic, generating the modified hydrostatic lattice constants simply requires applying the same percent change to all three independent directions.

We computed atomic-level strain-distribution profiles using the same Keating-type potentials[30] described and parameterized by Lee and Hwang.[14,15] The Keating-type valence-force model estimates strain energy ($E_{\rm strain}$) by summing deviations in both bond length and bond angles from perfect crystalline Si. Gradient shading each atom by either $E_{\rm strain}$ or bond length averaged over the four nearest neighbors yields useful three-dimensional profiles of the strain-field distribution throughout the model supercell. Scripts were generated in the Jmol scripting language[31] to map strain analysis data from DFT-optimized configurations to ionic coordinates for subsequent rendering in the open source Jmol viewer application.

In our recent work,[22] we reported orientation-dependent behavior for small self-interstitial clusters ($I_{\rm n}$, $n \leq 10$) under biaxial strain using the same ground-state configurations studied by Lee and Hwang.[14,15] Figure 2 shows these same clusters for reference that we used as the foundation for additional discoveries we report in this paper. Similar to the dual-response strain behavior observed for the I_4 compact cluster under biaxial strain, we observe orientation-dependent strain responses from other fourfold-coordinated clusters and also see cluster configuration changes under biaxial strain conditions of sufficient magnitude.

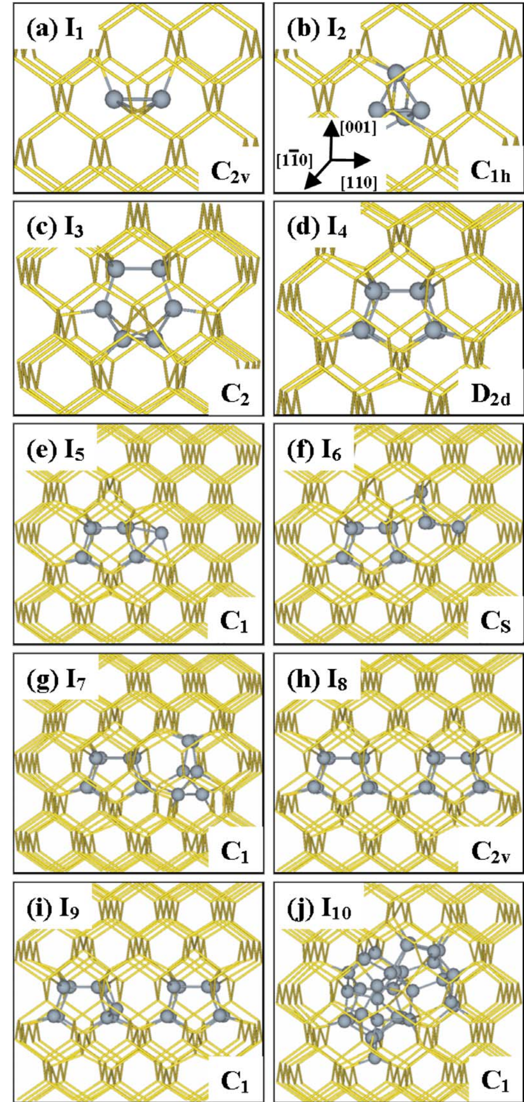

FIG. 2. (Color online) Ground-state configurations of small self-interstitial clusters ($I_{\rm n}$, $n \leq 10$) shown in their initial orientations with corresponding defect symmetries indicated. Light gray (gold) wireframe represents the bulk crystalline Si. Dark gray spheres represent interstitial atoms and their highly strained neighbors.

Various configurations of I_3 and the energetically stable I_4 cluster will be the focus of this paper as these clusters are seen to function as core building blocks for larger clusters, especially when strain conditions are present. Figure 3 shows the same fourfold-coordinated I_3 and I_4 clusters from Fig. 2 in their A-labeled orientations (see Fig. 4) isolated from the Si lattice in order to establish the salient shape and symmetry features to facilitate further discussion of cluster orientations. Henceforth, we will refer to this ground-state I_3 configuration as $I_3^{\rm g}$. Figure 3 shows the C_2 symmetry of $I_3^{\rm g}$ and the D_{2d} symmetry of I_4, as well as the symmetry axes that characterize their respective group symmetries.[32,33]

In our previous work,[22] we described how two cluster orientations are potentially relevant under biaxial strain using the exemplary features of the I_4 cluster core. In general, any initial cluster orientation can be transformed by interchang-

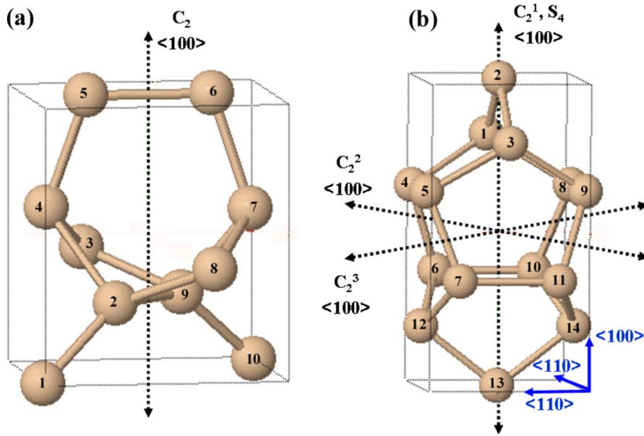

FIG. 3. (Color online) Cluster core and strained nearest neighbors that comprise (a) the C_2 symmetry of the I_3^g core and (b) the D_{2d} symmetry of the I_4 core shown isolated from crystalline Si in their respective A orientations. The crystallographic axes (blue) shown provide reference to the supercell orientation employed in both cases. In (a), the I_3^g configuration only has a single C_2-symmetry rotation axis shown in black. In (b), I_4 has three C_2-symmetry axes, each aligned with one of the ⟨100⟩ directions. Additionally, I_4 has a S_4 rotation-reflection axis that is collinear with the C_2^1 axis. The atoms shown are arbitrarily numbered to facilitate discussion.

ing alignment among the equivalent crystallographic directions. Using I_3^g as an example, the C_2 axis shown [Fig. 3] can be aligned with the [001], [010], or [100] directions. In our Si substrate orientation, only two orientations are potentially unique under biaxial strain, but all three are potentially unique in the more general case of uniform uniaxial strain. For some configuration symmetries, pure rotation about a symmetry axis may also change the cluster strain response. We will refer to orientation changes between equivalent directions as primary transformations and pure rotation orientation changes as secondary transformations for the remainder of this paper.

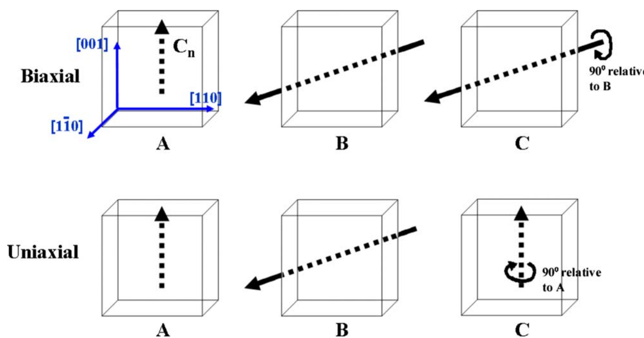

FIG. 4. (Color online) Pictorial reference to orientation nomenclature used in the text. An arbitrary C_n axis is assigned to the clusters in the initial orientations labeled A. A C_1-symmetry designation (Ref. 32) indicates no nontrivial symmetry operations are present, so, at minimum, a C_1 axis can be applied in an arbitrary fashion to any generic configuration. The B orientation is the same for both strain cases, while the C orientations represent pure rotations of the previous orientations, as indicated, that were found to modulate the strain response uniquely relative to either A or B. Biaxial strain is applied in our system in the plane containing [110] and [1$\bar{1}$0], while uniaxial strain is applied only along [110].

Figure 4 defines a simple orientation nomenclature for the various cases reviewed for biaxial and uniaxial strain in this work. Orientation C is often degenerate with orientation A with respect to uniaxial strain response; however, we have observed distinct behavior among all three orientations A, B, and C for clusters with significant structural components aligned along ⟨110⟩. For those cases, A and C orientations interchange ⟨110⟩ structural alignment between a state that is parallel with the applied strain and a state that is perpendicular to the applied strain. We also emphasize that the orientation-dependent strain behavior we report in this work highlights the most interesting orientations produced both through the integrated atomistic modeling procedure of Lee and Hwang[14–16] and manually-generated orientations produced through mathematical transformations of cluster configurations; therefore, not every conceivable orientation is represented.

III. RESULTS AND DISCUSSION

Comprehensive inspection of Fig. 2 shows that all ground-state configurations from I_1 through I_9 can be built using various combinations and orientations of only I_1 through I_4, which motivates further understanding of these structural components. Internally, all interstitial clusters are compressively strained and their disruptive presence to the periodicity of the Si lattice generates a localized nonuniform strain field. External strain applied to the Si lattice modulates virtually all material properties and the behavior of intrinsic defects. We characterize the energetic stability of interstitial clusters using formation energies dependent on both cluster size (n) and strain condition (ε) as follows:

$$E_f(n,\varepsilon) = E_{\text{tot}}(n,\varepsilon) - \frac{n+N}{N} E_{\text{bulk}}(\varepsilon), \tag{5}$$

where $E_{\text{tot}}(n,\varepsilon)$ is the total energy of the I_n cluster in the $n+N$ atom supercell, n is the size of the interstitial cluster, N is the basis number of atoms in the bulk Si supercell, and $E_{\text{bulk}}(\varepsilon)$ is the total energy of the N atom supercell of crystalline Si at a given strain condition. Unless noted otherwise, we report formation energies of clusters on a per interstitial atom basis.

A. Single interstitial (I_1)

In Fig. 5, we present formation energies for various configurations and orientations of I_1 under both biaxial and uniaxial strain conditions. The split-⟨110⟩ configuration is well-established as the neutral-state minimum-energy configuration in strain-free Si and we calculate its strain-free formation energy [$E_f(1,0\%)$] as 3.76 eV. However, our results suggest that the most favorable configuration changes to the tetrahedral configuration (T) under 4% compressive biaxial strain. At 4% compressive biaxial strain, E_f is 3.83 eV for T and 3.92 eV for the most favorable orientation of the split-⟨110⟩ configuration. The tetrahedral configuration of

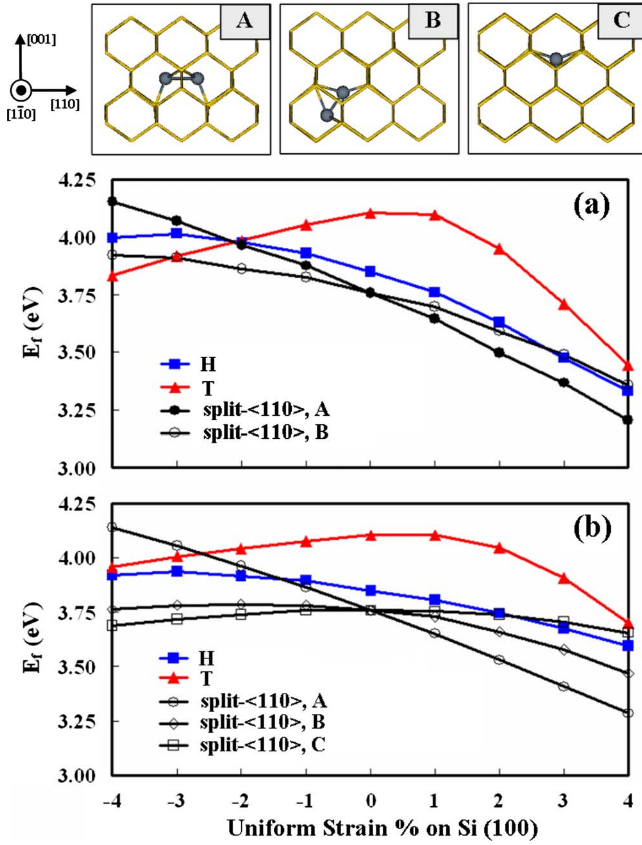

FIG. 5. (Color online) (a) Formation energy per interstitial for various I_1 configurations/orientations as a function of biaxial strain using $256+n$ supercells. Different configurations are grouped by color. Tensile strain is defined to be positive. The hexagonal configuration is denoted by "H" and the tetrahedral configuration is denoted by "T." (b) Formation energy per interstitial for various I_1 configurations/orientations as a function of uniaxial strain using $256+n$ supercells. (Upper panel) Various reference orientations of split-$\langle 110\rangle$ shown as viewed along $[1\bar{1}0]$. Light gray (gold) wireframe represents bulk Si atoms in the lattice. Dark gray spheres represent interstitial atoms and their highly strained neighbors.

I_1 is actually stabilized by biaxial strain of either sign since we observe the maximum formation energy $[E_f(1,0\%)=4.10\text{ eV}]$ for the strain-free case. Similar trends are observed in Fig. 5(b) for uniaxial strain, but T exhibits less stabilization under uniaxial strain relative to the biaxial case. In addition, Fig. 5(b) shows that uniaxial strain produces three unique $E_f(1,\varepsilon)$ responses for the split-$\langle 110\rangle$ configuration. Our results suggest that increased alignment of the split-$\langle 110\rangle$ bond with the direction of applied uniaxial strain ($[110]$) increases the sensitivity of the $E_f(1,\varepsilon)$ response.

B. Di-interstitial (I_2)

In Fig. 6, we present formation energies for various orientations of the I_2 configuration under both biaxial and uniaxial strain. While the $E_f(2,\varepsilon)$ responses for the two relevant orientations are degenerate for biaxial strain, we do observe an interesting distortion of the ground-state configuration at 4% compressive biaxial strain that disrupts the monotonically increasing $E_f(2,\varepsilon)$ trend as strain becomes increasingly compressive. Under uniaxial strain [Fig. 6(b)], we see the $E_f(2,\varepsilon)$ response is degenerate again for the A and B orientations, but the C orientation shows a more sensitive $E_f(2,\varepsilon)$ response. It is also apparent that uniaxial strain causes less $E_f(2,\varepsilon)$ change per unit change in strain than the biaxial case through comparison of the slopes of the respective $E_f(2,\varepsilon)$ trends for the A and B orientations of I_2.

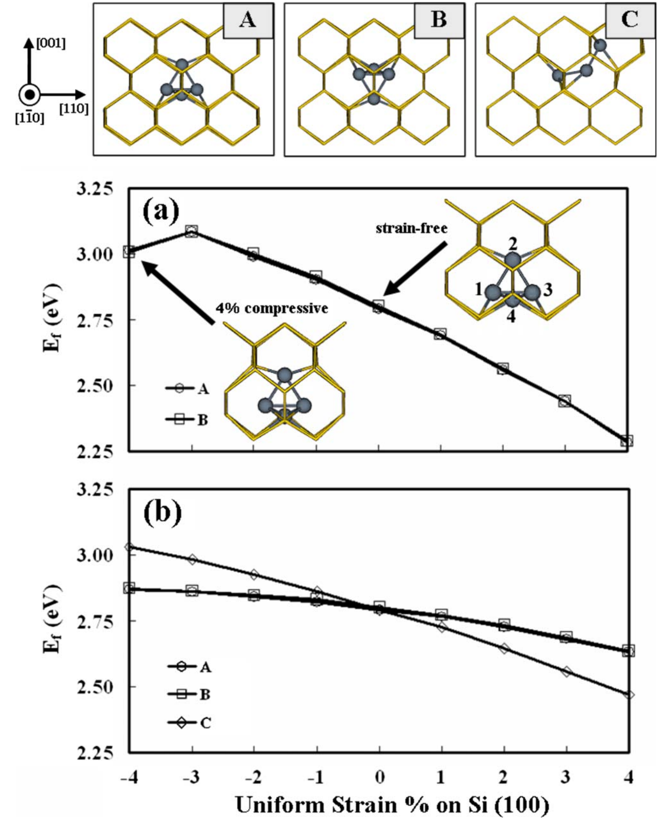

FIG. 6. (Color online) (a) Formation energy per interstitial for I_2 as a function of biaxial strain using $256+n$ supercells. The two orientations exhibit degenerate strain responses, but an interesting distortion of the configuration occurs for both orientations at 4% compressive strain. The insets contrast the two embedded I_2 configurations under 4% compressive and strain-free conditions. Atoms are arbitrarily numbered to facilitate discussion. Without strain, the triangle formed by atoms 1, 2, and 3 ($\triangle$ 123) is isosceles, with the short leg between atoms 1 and 3 measuring 2.29 Å and the long legs measuring 2.45 Å. Under 4% compressive strain, note that this same group of three atoms shifts up along $[001]$ with respect to the lattice, the 1–3 bond stretches to 2.42 Å, and the remaining legs shrink to 2.43 Å. Under 4% biaxial compression, $\triangle$ 123 becomes approximately equilateral. (b) Formation energy per interstitial for I_2 as a function of uniaxial strain using $256+n$ supercells. (Upper panel) Various reference orientations of I_2 shown as viewed along $[1\bar{1}0]$. Light gray (gold) wireframe represents bulk Si atoms in the lattice. Dark gray spheres represent interstitial atoms and their highly strained neighbors. Although initially unique, the B orientation of I_2 is sufficiently similar to A so that geometric optimization relaxes B back into A.

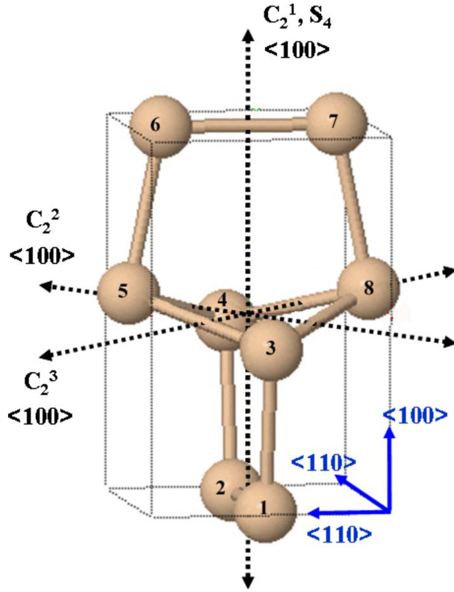

FIG. 7. (Color online) Cluster core and nearest neighbors that comprise the D_{2d} symmetry of the $I_3^{4\%c}$ structure shown isolated from crystalline Si. The A is orientation shown, which is destabilized as strain conditions become more tensile. Like I_4, this configuration has three C_2-symmetry axes (black), each aligned with $\langle 100 \rangle$ crystallographic directions. Additionally, there is an S_4 rotation-reflection axis that is collinear with the C_2^1 axis. The axes (blue) shown provide crystallographic reference to the supercell orientation. The atoms shown are arbitrarily numbered to facilitate discussion.

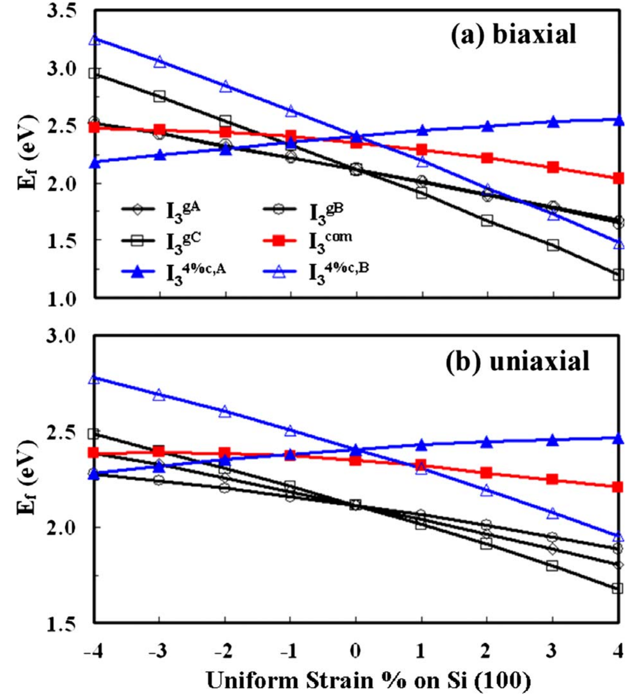

FIG. 8. (Color online) Formation-energy dependence per interstitial as a function of (a) biaxial strain and (b) uniaxial strain for various configurations and orientations of I_3 using $256+n$ supercells. Different configurations are grouped by color. I_3^{g} is the most stable configuration under all strain conditions investigated, except for highly compressive biaxial conditions ($\varepsilon \leq -2$), where the $I_3^{4\%c,A}$ structure orientation becomes most favorable.

C. Tri-interstitial (I_3)

Using the integrated atomistic modeling procedure of Lee and Hwang[14–16] with biaxial strain conditions, we identified unusual structures and orientations of Si interstitial clusters, including the configuration of I_3 in Fig. 7 that was formed under 4% compressive biaxial strain. The I_3 configuration we identified has D_{2d} symmetry, like the I_4 core structure, and also exhibits similar orientation-dependent strain behavior (*vide infra* Fig. 10) as previously detailed for I_4 (Ref. 22).

Figure 8 shows how $E_f(3,\varepsilon)$ varies with both biaxial and uniaxial strain for the array of configurations and orientations of I_3 we investigated, while Fig. 9 shows the corresponding single perspective views along $[1\bar{1}0]$ of each configuration/orientation. Note that these results extend those of our previous work[22] and illuminate the more subtle orientation-dependent stability of the ground-state I_3 configuration (I_3^{g}). In addition, Fig. 8(a) provides the $E_f(3,\varepsilon)$ response of the compact configuration of I_3 (I_3^{com}) and another I_3 configuration formed under 4% compressive biaxial strain conditions ($I_3^{4\%c}$). Over the range of biaxial strain conditions investigated ($-4 \leq \varepsilon \leq 4\%$), Fig. 8(a) suggests at least three configurations/orientations of the tri-interstitial could be observed, depending on the strain conditions present: (1) $I_3^{4\%c,A}$ under high compression $[-4 \leq \varepsilon \leq -2\%]$, (2) I_3^{gA} or I_3^{gB} under light compression to strain-free conditions $[-2 \leq \varepsilon \leq 0\%]$, and (3) I_3^{gC} for strain-free to highly tensile conditions $[0 \leq \varepsilon \leq 4\%]$. The C orientation of I_3^{g} was determined as the most energetically stable configuration of I_3 under 4% tensile biaxial strain. It is interesting that the $E_f(3,\varepsilon)$ biaxial response is identical for I_3^{gA} and I_3^{gB} but different for the secondary transformation of I_3^{gB} into I_3^{gC}. Further examination of each configuration shows that the 9–2 bond of I_3^{g} [Fig. 3(a)] is roughly within the plane of strain for both I_3^{gA} and I_3^{gB}, while the 9–2 bond is perpendicular to the plane of strain in I_3^{gC}.

We make two important observations about the orientation-dependent strain behavior of $I_3^{4\%c}$ from Fig. 8(a). First, $I_3^{4\%c}$ exhibits the largest difference in orientation-dependent biaxial strain response (by quantification of slopes) of any interstitial cluster we studied other than I_4. In correlation, $I_3^{4\%c}$ and I_4 are also the only structures studied that have dominant D_{2d} point-group symmetry (I_3^{com} is technically also D_{2d}, but the structure approximately exhibits higher-order T_d symmetry[22]). Second, $I_3^{4\%c,A}$ is the only structure orientation we studied that exhibits a positive slope for $E_f(n,\varepsilon)$ as a function of biaxial strain; as a result, $I_3^{4\%c,A}$ is the only structure orientation destabilized by tensile biaxial strain. Most interstitial clusters are stabilized under tensile conditions because the lattice becomes more accommodating to interstitial atoms as it stretches.

Figure 8(b) reveals similar trends for the I_3 structures subjected to uniaxial strain. A notable departure in the uniaxial case includes splitting of the degeneracy in the $E_f(3,\varepsilon)$ responses of I_3^{gA} and I_3^{gB}. Furthermore, the I_3^{g} orientations are energetically more favorable than the $I_3^{4\%c}$ orientations under uniaxial strain of either sign relative to equivalent magni-

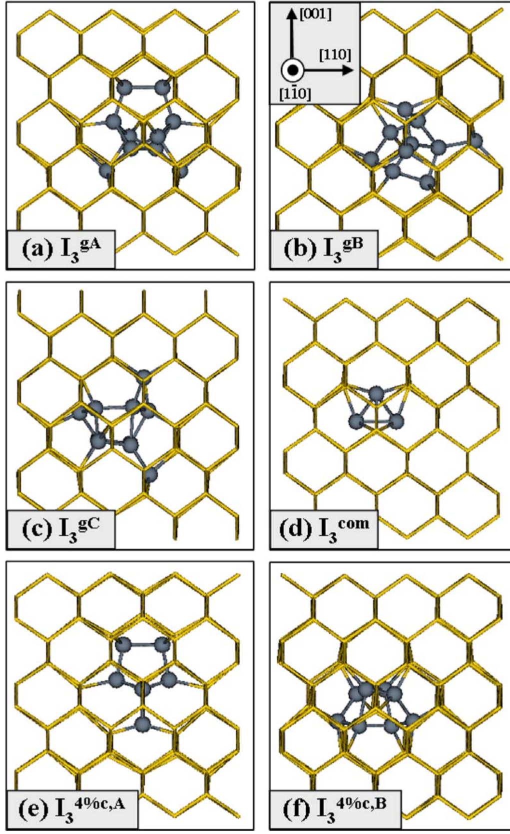

FIG. 9. (Color online) Various strain-free configurations and orientations of the I_3 cluster embedded inside subsections of their respective 256-atom supercells as viewed along [1$\bar{1}$0]. Symmetries for each configuration are C_2, T_d (approximate), and D_{2d} for I_3^g, I_3^{com}, and $I_3^{4\%c}$, respectively. Light gray (gold) wireframe represents bulk Si atoms in the lattice. Dark gray spheres represent the interstitial atoms and their highly strained neighbors. For each unique configuration, the same number of atoms are represented as spheres to aid comparison across different orientations.

tudes of biaxial strain. While the $I_3^{4\%c,A}$ structure is favored under 4% biaxial compression, the energetic advantage is gone under 4% uniaxial compression [$E_f(3,-4\%)=2.28$ eV for both I_3^{gB} and $I_3^{4\%c,A}$]. In general, the effect of strain on $E_f(3,\varepsilon)$ responses is diminished for the uniaxial case relative to the biaxial case as evidenced by a reduction in the absolute value of the slope for the uniaxial $E_f(3,\varepsilon)$ response curves; as a result, the difference in strain-free formation energies is more dominant in the uniaxial case in evaluation of the relative stability of two structures subjected to the same strain conditions.

D. Tetra-interstitial (I_4)

We extend our previous study[22] of I_4 by examining the $E_f(n,\varepsilon)$ responses under uniaxial, biaxial, and hydrostatic strain for the primary orientations [Fig. 4] and present these results in Fig. 10. $E_f(n,\varepsilon)$ responses are approximately linear for all orientations and strain types studied for I_4. For the strain-free case, we find $E_f(4,0\%)$ is 1.89 eV. For I_4^A, the $E_f(4,\varepsilon)$ responses to strain are identical and nearly invariant

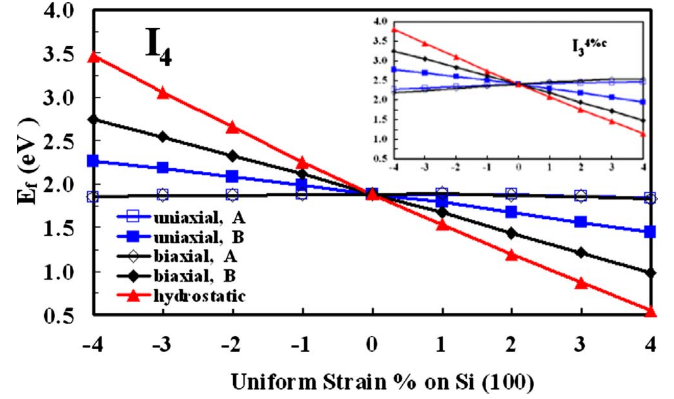

FIG. 10. (Color online) Formation-energy dependence per interstitial of I_4 with D_{2d} symmetry shown for primary orientations and different types of strain conditions using 256+n supercells. Strain types are grouped by color. For comparison, the inset shows the same information obtained for the $I_3^{4\%c}$ structure, which also has D_{2d} cluster symmetry. $I_3^{4\%c}$ shows all the same trends in formation-energy response behavior to various strain conditions as I_4.

for both the uniaxial and biaxial conditions. On the other hand, the $E_f(4,\varepsilon)$ curves for I_4^B both show sensitivity to strain, but the uniaxial response to strain is weaker than the biaxial response. The slope of the biaxial $E_f(n,\varepsilon)$ response of orientation B is a factor of 2 greater than the slope of the uniaxial $E_f(n,\varepsilon)$ response. The hydrostatic $E_f(4,\varepsilon)$ response of I_4 is the most sensitive to changes in strain among all strain types and orientations considered. Of most interest is the strong stabilizing effect predicted if hydrostatic tension is present. Overall, a trend is observed for increased strain sensitivity as conditions vary from uniaxial to biaxial to hydrostatic strain. In consequence, the cluster formation energies become more sensitive to strain as the degrees of freedom in volumetric relaxation of bulk Si are reduced.

Expecting that the $I_3^{4\%c}$ structure might exhibit analogous behavior in the presence of strain because of its shared D_{2d} symmetry classification with I_4, we present that same $E_f(n,\varepsilon)$ data in the inset of Fig. 10 for comparison. For the strain-free case, $E_f(3,0\%)$ is 2.41 eV for $I_3^{4\%c}$. From Fig. 10, $I_3^{4\%c}$ shows all the same $E_f(n,\varepsilon)$ trends as I_4 in correlation with its shared D_{2d} symmetry classification.

E. I_3+I_4 aggregation

The intricacies of the previously reported I_7 structure[14] provide an excellent example of the effect that biaxial strain may have on the development of larger interstitial clusters from the core I_3 and I_4 component clusters, as well as configurational changes that can occur during assembly of larger clusters. Figure 11 presents the $E_f(7,\varepsilon)$ biaxial strain responses of four different configurations/orientations of the I_7 cluster and Fig. 12 shows the corresponding single perspective views of each structure as viewed along [1$\bar{1}$0]. Figures 12(a)–12(c) represent three orientations of the ground-state I_7 configuration [Fig. 2(g)] which we will designate as I_7^g for the remainder of this paper. Figure 12(d) shows the most stable structure under 4% compressive biaxial strain ($I_7^{4\%c}$) as

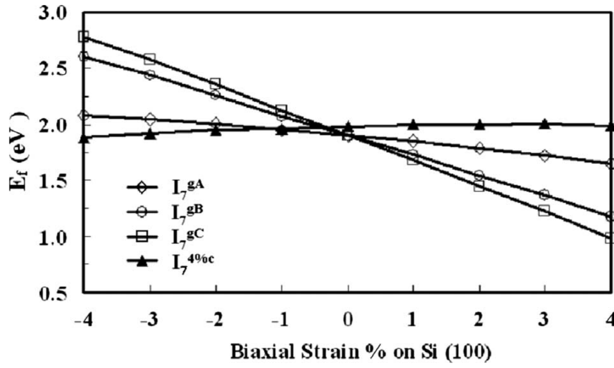

FIG. 11. Formation-energy dependence per interstitial as a function of biaxial strain for various configurations/orientations of the I_7 cluster using $480+n$ supercells. The ground-state configurations (I_7^{g}) are composed of I_4 and I_3^{g}, while $I_7^{4\%\mathrm{c}}$ is composed of I_4 and $I_3^{4\%\mathrm{c}}$. Only the A orientation of $I_7^{4\%\mathrm{c}}$ is represented here.

determined using the procedure of Lee and Hwang.[14–16] From these structures, it is apparent that I_7 is constructed from the I_3 and I_4 cores discussed and the configuration of the I_3 core component is additionally dictated by the strain conditions present. Like the I_3 case, we identified the I_7^{gC} orientation as the most stable structure under 4% tensile biaxial strain. For I_7^{g}, the $E_f(7,0\%)$ is 1.90 eV, while $E_f(7,0\%)$ is 1.98 eV for $I_7^{4\%\mathrm{c}}$. Only the A orientation of $I_7^{4\%\mathrm{c}}$ was reviewed. In analogy with our I_3 results, the presence of $I_3^{4\%\mathrm{c,A}}$ in $I_7^{4\%\mathrm{c,A}}$ produces a $E_f(7,\varepsilon)$ strain response that shows slightly decreased stability under tensile conditions and the C

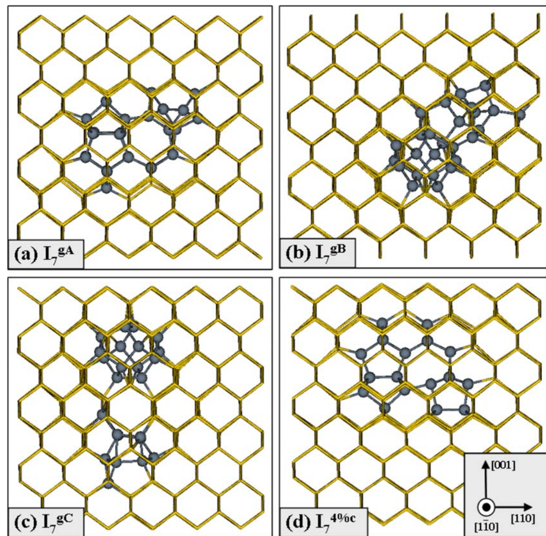

FIG. 12. (Color online) Various strain-free configurations and orientations of the I_7 cluster embedded inside their respective 480-atom supercells as viewed along $[1\bar{1}0]$. Light gray (gold) wireframe represents bulk Si atoms in the lattice. Dark gray spheres represent the interstitial atoms and their highly strained neighbors. Each variant of I_7 shown is effectively constructed from constituent I_3 and I_4 core components as follows: (a) $I_4^{\mathrm{A}}+I_3^{\mathrm{gA}}$, (b) $I_4^{\mathrm{B}}+I_3^{\mathrm{gB}}$, (c) $I_4^{\mathrm{B}}+I_3^{\mathrm{gC}}$, and (d) $I_4^{\mathrm{A}}+I_3^{4\%\mathrm{c,A}}$. Note that various degrees of degeneracy in biaxial strain response are possible, so constituent I_3 cores shown here in I_7 are in some cases flipped, mirrored, and/or rotated 90° about [001] from the I_3 core perspectives depicted in Fig. 9.

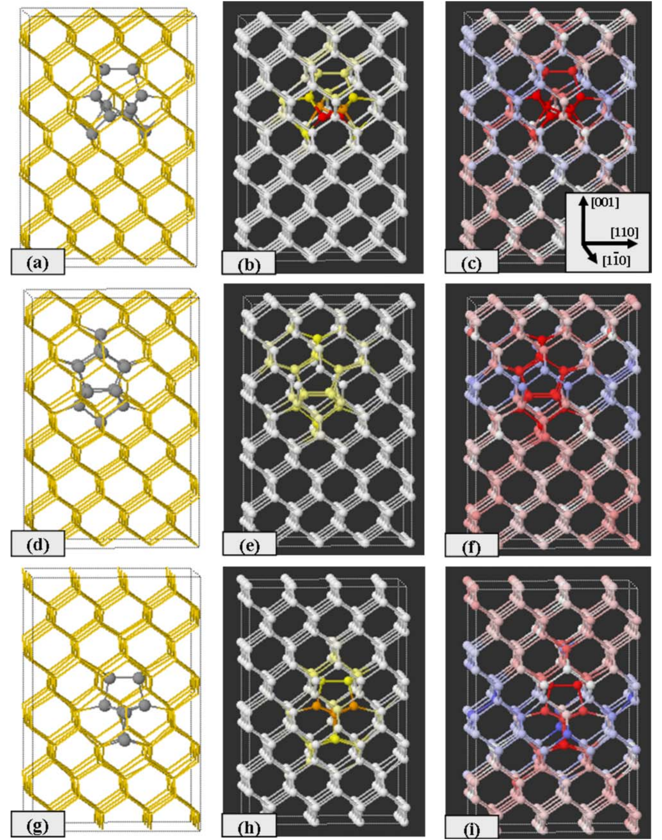

FIG. 13. (Color online) Atomic-level strain-distribution profiles shown for strain-free configurations of I_3^{gA}, I_4^{A}, and $I_3^{4\%\mathrm{c,A}}$. The subfigures of the left column highlight each configuration embedded inside 256-atom supercells. Light gray (gold) wireframe represents bulk Si atoms in the lattice. Dark gray spheres represent the interstitial atoms and their highly strained neighbors. The images in the central column are strain profiles based on E_{strain}. Gradient shading is effectively normalized for all strain profiles shown by calibrating the color spectrum to span all values observed across all structures. For the E_{strain} profiles of the central column, the color varies using the WYOR spectrum as E_{strain} increases from 0 to 0.66 eV. The subfigures of the right column are based on average bond length. Each atom is assigned an average bond length based on the four bonds formed with its nearest neighbors and is gradient shaded accordingly. The color varies using the RWB spectrum as the average bond lengths shift from compressive to strain-free to tensile. The RWB spectrum used covers the Si-Si DFT equilibrium bond length of 2.36 ± 0.07 Å.

orientation of I_7^{g} is the most stable under tensile conditions. Unlike our I_3 results, the A and B orientations of I_7^{g} are not degenerate with respect to $E_f(7,\varepsilon)$ response, which is likely attributable to the dual-response behavior influenced by the presence of the I_4 core.

F. Local strain distributions

To further characterize interstitial clusters, we present atomic-level strain-distribution profiles that depict the localized strain fields induced by clusters. In Fig. 13, we present strain-distribution profiles based on both strain energy (E_{strain}) and average bond length for I_3^{g}, $I_3^{4\%\mathrm{c}}$, and I_4, all in the

A orientation. The hybrid ball-and-stick/wireframe images are shown to highlight the cluster configurations [left column Fig. 13]. Strain energies from the Keating-type parameterization of the Si system from Lee and Hwang[14,15] were used to gradient shade the profiles using a color spectrum that shifts from white to yellow to orange to red (WYOR) as E_{strain} increases [middle column Fig. 13]. Strain profiles based on average bond length [right column Fig. 13] are easy to construct for a fourfold-coordinated system. The color spectrum in these profiles shifts from red to white to blue (RWB) as the average bond lengths shift from compressive to strain-free to tensile. The RWB spectrum covers the Si-Si DFT equilibrium bond length of 2.36 ± 0.07 Å. The E_{strain} profiles are useful to identify the locations that have the highest magnitude of strain, while the profiles based on average bond length are convenient to assess the sign of strain present (compressive/tensile). To facilitate comparison among clusters, the color spectrums are effectively normalized for E_{strain} and average bond length, respectively, across all three clusters.

In a normalized context, the E_{strain} profiles qualitatively indicate that the most strained atoms among the three clusters are in I_3^g [Fig. 13(b)] because two of the atoms are red. Referring to Fig. 3(a), these are atoms labeled "9" and "2" and they both have $E_{strain}=0.66$ eV. Recall that the orientation of the I_3^g 9–2 bond with respect to the plane of strain corresponds to the orientation-dependent $E_f(3,\varepsilon)$ response. For comparison, the maximum values of E_{strain} are 0.47 and 0.31 eV for the $I_3^{4\%c}$ and I_4 clusters, respectively. The well-known local $E_f(4,0\%)$ minima[6,7] of I_4 relative to other small clusters is likely attributable to the success of the I_4 configuration in E_{strain} minimization. From symmetry, the strain-free maxima of E_{strain} for I_4 are seen at both atom 2 and atom 13. For $I_3^{4\%c}$, the strain-free maxima of E_{strain} are seen simultaneously at these atoms: 3, 4, 5, and 8. Considering the profiles based on average bond length, we can ascertain additional qualitative information about the local environment surrounding each cluster. The interior regions of all clusters are highly compressive (red), but much of the immediate cluster interface with bulk Si is under net tensile strain (blue). These $256+n$ supercells employed would need to be enlarged significantly in both [110] and $[1\bar{1}0]$ directions to comment further on the anisotropic nature of the localized tensile strain field generated around each interstitial configuration.

G. Electronic structure

We provide some electronic-structure characterization of small interstitial clusters by presenting results we found on the total DOS (TDOS) of selected clusters under strain-free conditions. In particular, we anticipate that the fourfold-coordinated configurations of I_3^g, $I_3^{4\%c}$, and I_4 will be less likely than clusters with dangling bonds to introduce new states in the Si band gap, which is generally detrimental to electrical device performance. Figure 14 shows the TDOS results we obtained. Each subfigure in Fig. 14 compares the TDOS for bulk Si relative to various embedded interstitial clusters. In Fig. 14(a), the presence of the split-⟨110⟩ configuration introduces a large concentration of states in the band gap near the conduction-band minimum. For I_2, the band gap (E_g) is significantly narrowed relative to bulk Si and the number of states just below the valence-band maximum (VBM) is also decreased. For I_3^g, the TDOS closely resembles that of bulk Si and Eg is relatively unchanged as well. The I_3^{com} structure exhibits similar departures from the bulk Si TDOS as seen for I_2, including E_g reduction relative to bulk Si. $I_3^{4\%c}$ shows a modest band-gap reduction and an increase in states just below VBM. For I_4, we do observe some E_g reduction; otherwise, the TDOS for I_4 in and around the band gap is similar to bulk Si. Note that no significant orientation effect was seen for I_4 in terms of TDOS, as expected. The reduction in E_g, even for the fourfold-coordinated structure of I_4, is consistent with the introductory proposal of the D_{2d} configuration of I_4 by Arai *et al.*[34] In that work, they generalize that significant distortions in the Si-Si bond length can introduce localized states just inside the bulk E_g, even in the absence of dangling bonds. In summary, our results confirm that fourfold-coordinated clusters (I_3^g, $I_3^{4\%c}$, and I_4) generally exhibit less departure in TDOS from that of bulk Si relative to clusters that do not contain fourfold-coordinated bond topologies (split-⟨110⟩, I_2, and I_3^{com}).

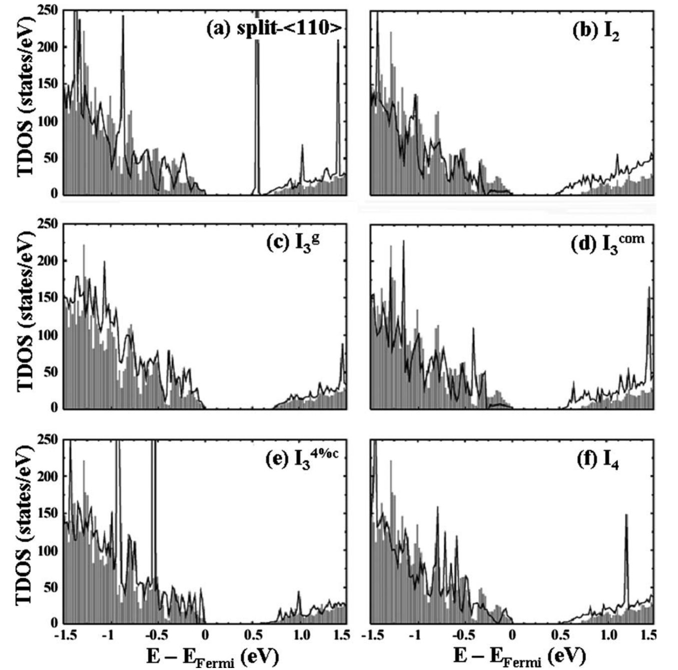

FIG. 14. TDOS near the Si band gap for various small interstitial clusters (black) using strain-free $256+n$ supercells with reference to a 256-atom bulk Si supercell (gray background). Each different structure references its own calculated Fermi level so that all cases have VBM set to zero.

IV. CONCLUSIONS

The energetic stability of neutral, compact interstitial clusters (I_n, $n \leq 4$) was investigated using first-principles DFT calculations for various orientations and configurations under different uniform strain conditions. Cluster sizes n

≤ 4 were selected for their role in forming larger clusters. The results of our biaxial and uniaxial strain condition ($-4 \leq \varepsilon \leq 4\%$) investigation reveal that the minimum-energy orientation and/or configuration is a function of the strain conditions present in the system. While our investigation includes results from simulated conditions that are relatively extreme ($|\varepsilon| \geq 1$) for conventional strained CMOS processes, we feel that our exploration of configuration changes and the impact of the orientation effect under strained conditions is of considerable scientific value for understanding and designing strained materials. For I_1, the tetrahedral structure becomes the minimum-energy configuration for 4% compressive biaxial strain. The I_2 cluster undergoes a distortion in configuration at 4% compressive biaxial strain that lowers the expected formation energy predicted by the ground-state configuration. Application of biaxial strain conditions during the cluster formation modeling process revealed a previously unreported configuration of I_3 ($I_3^{4\%c}$) with D_{2d} symmetry. The D_{2d} symmetry configurations of $I_3^{4\%c}$ and I_4 exhibit analogous formation-energy response behavior under uniaxial, biaxial, and hydrostatic strain conditions. $I_3^{4\%c}$ also shows a strong dual-response formation energy behavior, like I_4, for the two relevant orientations under biaxial strain conditions. The $I_3^{4\%c}$ configuration is the only Si interstitial cluster investigated that is destabilized as strain conditions become more tensile. Cluster energetic dependence on uniaxial strain is often similar, but less sensitive, to that seen under biaxial strain, but uniaxial strain conditions often break orientation-dependent degeneracies observed under biaxial conditions. Under biaxial strain conditions, I_7 exemplifies the significance of the I_3 and I_4 cores in the formation of larger clusters. In addition, the orientations (I_4 and I_3) and configurations (I_3) of the constituent cores of I_7 under biaxial strain follow the energetic trends seen for the isolated core components. We extend interstitial cluster characterization by providing atomic-level strain-distribution profiles in fourfold-coordinated systems using both calculated strain energies and strain based on average bond lengths to nearest neighbors. Finally, we present total density of states results that qualitatively confirm that interstitial clusters with fourfold coordination generally introduce less changes in and around the Si band gap than clusters without complete fourfold-coordinated bond topology.

ACKNOWLEDGMENTS

We acknowledge the Semiconductor Research Corporation (Grant No. 1413–001), the National Science Foundation (Grant No. CAREER-CTS-0449373), and the Robert A. Welch Foundation (Grant No. F-1535) for their financial support. We would also like to thank the Texas Advanced Computing Center for use of their computing resources.

*Author to whom correspondence should be addressed; gshwang@che.utexas.edu

[1] S. E. Thompson, Guangyu Sun, Youn Sung Choi, and Toshikazu Nishida, IEEE Trans. Electron Devices **53**, 1010 (2006).
[2] J. Kim, F. Kirchhoff, J. W. Wilkins, and F. S. Khan, Phys. Rev. Lett. **84**, 503 (2000).
[3] P. K. Giri, Semicond. Sci. Technol. **20**, 638 (2005).
[4] J. Kim, J. W. Wilkins, F. S. Khan, and A. Canning, Phys. Rev. B **55**, 16186 (1997).
[5] M. Kohyama and S. Takeda, Phys. Rev. B **46**, 12305 (1992).
[6] C. J. Ortiz, P. Pichler, T. Fuhner, F. Cristiano, B. Colombeau, N. E. B. Cowern, and A. Claverie, J. Appl. Phys. **96**, 4866 (2004).
[7] N. E. B. Cowern, G. Mannino, P. A. Stolk, F. Roozeboom, H. G. A. Huizing, J. G. M. van Berkum, F. Cristiano, A. Claverie, and M. Jaraiz, Phys. Rev. Lett. **82**, 4460 (1999).
[8] K. Derbyshire, Solid State Technol. **50**, 38 (2007).
[9] K.-J. Chui, K.-W. Ang, N. Balasubramanian, M.-F. Li, G. S. Samudra, and Y.-C. Yeo, IEEE Trans. Electron Devices **54**, 249 (2007).
[10] D. J. Paul, Semicond. Sci. Technol. **19**, R75 (2004).
[11] R. Harper, Mater. Sci. Eng., B **134**, 154 (2006).
[12] D. Yu, S. Lee, and G. S. Hwang, J. Appl. Phys. **102**, 084309 (2007).
[13] A. Thean and J. P. Leburton, Appl. Phys. Lett. **79**, 1030 (2001).
[14] S. Lee and G. S. Hwang, Phys. Rev. B **77**, 085210 (2008).
[15] S. Lee and G. S. Hwang, Phys. Rev. B **78**, 045204 (2008).
[16] S. Lee and G. S. Hwang, Phys. Rev. B **78**, 125310 (2008).
[17] J. P. Perdew, K. Burke, and M. Ernzerhof, Phys. Rev. Lett. **77**, 3865 (1996).
[18] J. P. Perdew and Y. Wang, Phys. Rev. B **45**, 13244 (1992).
[19] G. Kresse and J. Hafner, Phys. Rev. B **47**, R558 (1993); **49**, 14251 (1994); G. Kresse and J. Furthmüller, Comput. Mater. Sci. **6**, 15 (1996); Phys. Rev. B **54**, 11169 (1996).
[20] G. Kresse and J. Furthmüller, *VASP the Guide* (Vienna University of Technology, Vienna, 2001).
[21] D. Vanderbilt, Phys. Rev. B **41**, 7892 (1990).
[22] R. J. Bondi, S. Lee, and G. S. Hwang, Phys. Rev. B **79**, 104106 (2009).
[23] J. Singh, *Physics of Semiconductors and Their Heterostructures* (McGraw-Hill, New York, 1993).
[24] L. Lin, T. Kirichenko, B. R. Sahu, G. S. Hwang, and S. K. Banerjee, Phys. Rev. B **72**, 205206 (2005).
[25] P. Bhattacharya, *Semiconductor Optoelectronic Devices* (Prentice-Hall, Upper Saddle River, NJ, 1997).
[26] C. G. Van de Walle and R. M. Martin, Phys. Rev. B **34**, 5621 (1986).
[27] M. E. Levinshtein, S. L. Rumyantsev, and M. S. Shur, *Handbook Series on Semiconductor Parameters* (World Scientific, London, 1996), Vol. 1, p. 29.
[28] W. A. Brantley, J. Appl. Phys. **44**, 534 (1973).
[29] J. J. Wortman and R. A. Evans, J. Appl. Phys. **36**, 153 (1965).
[30] Y. Tu, J. Tersoff, G. Grinstein, and D. Vanderbilt, Phys. Rev. Lett. **81**, 4899 (1998).
[31] R. Hanson, 2008, Jmol Interactive Scripting Documentation: http://chemapps.stolaf.edu/jmol/docs/
[32] T. Engel and P. Reid, *Physical Chemistry* (Pearson Education, New York, 2006).
[33] N. W. Ashcroft and N. D. Mermin, *Solid State Physics* (Thomson Learning, USA, 1976).
[34] N. Arai, S. Takeda, and M. Kohyama, Phys. Rev. Lett. **78**, 4265 (1997).